PHYSICAL REVIEW B **104**, 174442 (2021)

Magnetic spin order in the honeycomb structured $Pb_6Co_9(TeO_6)_5$ compound

I. Panneer Muthuselvam,[1,*] K. Saranya,[2] Deepa Kasinathan,[3] R. N. Bhowmik,[4,†] R. Sankar,[5,6]
Namasivayam Dhenadhayalan,[7] G. J. Shu,[6,8] Wei-tin Chen,[6] L. Kavitha,[2] and King-Chuen Lin[7]
[1]*Department of Physics (MMV), Banaras Hindu University, Varanasi 221005, Uttar Pradesh, India*
[2]*Department of Physics, School of Basic and Applied Sciences,*
Central University of Tamil Nadu, Neelakudi, Thiruvarur 610005, Tamil Nadu, India
[3]*Max-Planck Institute for Chemical Physics of Solids, Nöthnitzer Strasse 4001187 Dresden, Germany*
[4]*Department of Physics, Pondicherry University, R. Venkataraman Nagar, Kalapet, Pondicherry 605014, India*
[5]*Institute of Physics, Academia Sinica, Taipei 10617, Taiwan*
[6]*Center for Condensed Matter Sciences, National Taiwan University, Taipei 10617, Taiwan*
[7]*Department of Chemistry, National Taiwan University,*
and Institute of Atomic and Molecular Sciences, Academia Sinica, Taipei 10617, Taiwan
[8]*Department of Materials and Mineral Resources Engineering, Institute of Mineral Resources Engineering,*
National Taipei University of Technology, Taipei 10608, Taiwan

(Received 28 January 2021; revised 2 September 2021; accepted 15 November 2021; published 29 November 2021)

We present a comprehensive experimental and theoretical study of the structural, electronic, magnetic, and thermodynamic properties of a $Pb_6Co_9(TeO_6)_5$ single crystal. The $Pb_6Co_9(TeO_6)_5$ crystal has shown a unique type of magnetic spin-lattice coupling, in which the lattice structure consists of four different Co ions sites with distorted octahedral coordinations. The x-ray photoelectron spectroscopy (XPS) results confirmed the oxidation states of Pb, Co, Te, and O elements in the sample. Moreover, XPS spectra revealed the adsorbed oxygen in the defect/vacancy sites of the lattice structure. The dc magnetization measurements exhibited a complex magnetic behavior with ferrimagnetic (FIM) transition with Curie temperature T_C at $\sim$21 K. At lower magnetic fields H, the zero-field-cooled and field-cooled curves showed a broad hump at $\sim$10.8 K and a shoulder peak at $\sim$6.2 K, which are suppressed at higher magnetic fields. The ac susceptibility data indicated spin-glass-like features. The heat capacity C_P measurements confirmed the FIM transition at T_C at $\sim$21 K, but without any trace of additional peaks at lower temperatures. The estimated Curie-Weiss constant θ_{CW} showed a peculiar field-dependent behavior along the $H \parallel c$ direction of the single crystal, where θ_{CW} is less field dependent for the $H \perp c$ direction. A large coercivity (13 kOe) is observed at 2 K for $H \parallel c$, whereas the magnetization curve of the single crystal is dominated by an antiferromagnetic feature for $H \perp c$. The behaviors indicate the anisotropy nature of the exchange interactions in the compound. The local spin density approximation + U total energy calculations were performed for various collinear spin configurations of a classical Heisenberg model in order to obtain the magnetic exchange interactions J_i at different distances for different neighbors.

DOI: 10.1103/PhysRevB.104.174442

I. INTRODUCTION

Magnetic materials with a frustrated spin-lattice structure have received considerable interest in the last few decades. Honeycomb magnetic lattices, e.g., $A_3Co_2SbO_6$ (A = Na, Ag, Li), have received much attention because they exhibit a rich variety of unusual quantum magnetic ground states, in which magnetic spin order can be treated as quasi-two-dimensional magnets within *a-b* planes and quasi-Ising magnets along the *c* axis of the crystal structure [1–6]. An ideal honeycomb lattice structure with antiferromagnetic (AFM) nearest-neighbor interaction J_1 should exhibit a long-range ground state without showing any frustration. On the other hand, competition between the second (J_2) and third (J_3) exchange interactions in honeycomb-type lattices leads to a complex magnetic state and spin frustration. Depending on the signs and ratio of J_2/J_1 and J_3/J_1, different types of spin order (e.g., Neel, zigzag, stripy, and spiral order) can be realized in honeycomb-type lattices [7]. Experimental results have shown the absence of long-range magnetic order in the ground state for some honeycomb lattice systems, such as $Na_3LiFeSbO_6$, Na_4FeSbO_6, and Li_4MnSbO_6 [8,9]. This is due to increasing lattice disorder (distortion) and spin frustration in the system. Koteswararao *et al.* [10] and Baral *et al.* [11] studied the magnetic properties of polycrystalline samples of $Pb_6Ni_9(TeO_6)_5$, which exhibited a weak ferromagnetic (FM) transition at $T_C \sim 24$ K, and canted AFM ground state was realized due to the presence of the Dzyaloshinskii-Moriya interactions. A relatively less studied compound, $Pb_6Co_9(TeO_6)_5$, is an isostructure of $Pb_6Ni_9(TeO_6)_5$.

The compound $Pb_6Co_9(TeO_6)_5$ adopts a hexagonal structure with space group $P6_322$ [a = 10.3915(1) Å, c =

---

[*] ipmphysics@gmail.com
[†] rnbhowmik.phy@pondiuni.edu.in

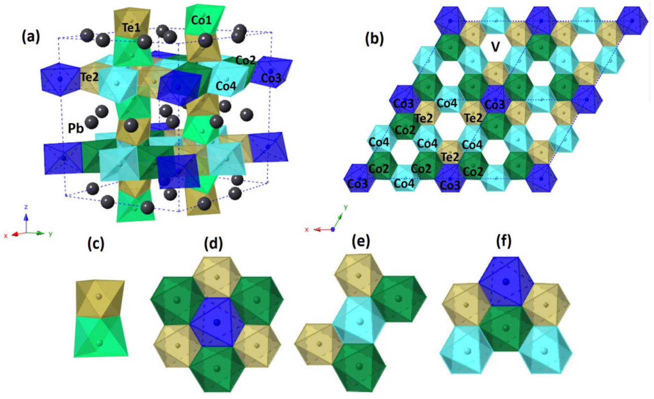

FIG. 1. (a) Schematic representation of the crystal structure of $Pb_6Co_9(TeO_6)_5$ and face-sharing Te1-Co1 octahedra corner shared with honeycomblike layers. The solid black spheres represent Pb atoms. (b) A-type honeycomb layer in the *a-b* plane. All intralayer octahedra are edge-shared octahedra. V corresponds to vacancies. The four different environmental symmetry of the oxygen distribution surrounding the Co center: (c) Te1-Co1, (d) Co3 center, (e) Co4 center, and (f) Co2 center.

13.6373(2) Å] [12]. A typical three-dimensional crystal structure of $Pb_6Co_9(TeO_6)_5$ is depicted in Fig. 1(a). As demonstrated by Artner and Weil [12], the structural unit contains two Pb atoms, four Co atoms, two Te atoms, and six O atoms. The four Co (CoO_6) and two Te (TeO_6) atoms occupy the octahedral environment with slightly distorted atomic positions. The crystal structure can be subdivided into two (A and B) types of layers that stack alternatively along the *c* axis. The first (type A) layer at $z \approx 0.25$ is made up of edge-sharing CoO_6 and TeO_6 octahedra, with 1/6 of the unoccupied octahedral holes (V). The edge-sharing CoO_6 octahedra form regular honeycomb-type lattices of Co2 and Co4 ions with corner-shared TeO_6 octahedra, with one at the top center and another one at the bottom center of the A-type honeycomb layer [shown in Fig. 1(b)]. The second (type B) layer at $z \approx 0$ consists of face-sharing CoO_6 and TeO_6 octahedra and a surrounding arrangement of Pb atoms. The two types of layers are linked together by corner sharing of CoO_6 and TeO_6 octahedra, with corner-shared CoO_6 (Co1) at the top center and at bottom center of the honeycomb lattices. The ion pairs (Co2 and Co3, Co2 and Co4, Co1 and Co4) form strong (Co-O-Co) superexchange couplings. The Co1 ions can be connected to Co2, Co3, and Co4 ions through nonmagnetic Te^{2+} ($4d^{10}$) ions by weak interlayer (Co-O-Te-O-Co) superexchange couplings.

Although the magnetic susceptibility of powdered $Pb_6Co_9(TeO_6)_5$ samples has been reported [10], a detailed study of the magnetic properties of a single crystal of $Pb_6Co_9(TeO_6)_5$ is absent in the literature. The present work reports the magnetic properties of single crystals compared with powdered crystals of the $Pb_6Co_9(TeO_6)_5$ compound. The experimental results from the magnetization measurements are complemented with heat capacity measurement and theoretical calculations. Both experimental and theoretical results suggest a rich variety of magnetic properties and a nonunique magnetic ground state, which are generally exhibited in low-dimensional transition metal oxides [1,13–16].

II. EXPERIMENTAL DETAILS

Single crystals of $Pb_6Co_9(TeO_6)_5$ were grown using a TeO_2 self-flux growth technique. High-purity (>99.9) PbO (1.281 g, 5.7 mmol), CoO (0.216 g, 2.9 mmol), and TeO_2 (0.914 g, 5.7 mmol) in the proper stoichiometric ratio were ground and thoroughly mixed, following the method described in Ref. [12]. The mixed powder was placed into an alumina crucible and heated to 800 °C at a rate of 80 °C/h and then held for 48 h at this temperature. The sample was then cooled down at a rate of 2 °C/h to 650 °C, followed by rapid cooling to room temperature. The heat-treated mixture was placed in distilled water to remove flux, and eventually, $Pb_6Co_9(TeO_6)_5$ and Pb_2CoTeO_6 crystals were obtained. In order to determine the crystal plane, the x-ray diffraction (XRD) pattern of the single crystal was recorded using Cu $K\alpha$ radiation at room temperature. The structure and phase purities of the ground single crystals (powder sample) were also confirmed by powder x-ray diffraction (XRD) using high-resolution synchrotron radiation at $\lambda = 0.619925$ Å. The XRD patterns were obtained with the Microstrip sYstem for Time-rEsolved experimeNts detector with a 15 keV beam at beamline 09A, Taiwan Photon Source, National Synchrotron Radiation Research Center. The powder sample was packed in a 0.1 mm borosilicate capillary, and the capillary was kept spinning during data collection. The x-ray photoelectron spectroscopy (XPS) analysis was carried out using a VG Scientific ESCALAB 250 spectrometer. The XPS measurement was carried out to determine the chemical composition and oxidation state of the elements in the $Pb_6Co_9(TeO_6)_5$ single crystal. The dc and ac susceptibility properties were studied using a commercial superconducting quantum interference device vibrating sample magnetometer. The temperature-dependent heat capacity was measured by a Quantum Design physical parameter measurement system.

III. CALCULATION DETAILS

The band structure calculations, based on density functional theory (DFT), were performed using a full-potential nonorthogonal local orbital code (FPLO) within the local (spin) density approximation [L(S)DA] [17,18]. The Perdew and Wang flavor [19] of the exchange-correlation potential was chosen for the scalar relativistic calculations. A strong on-site Coulomb repulsion of the Co $3d$ orbital was taken into account using the LSDA+U method, applying the "atomic limit" double-counting term. The projector on the correlated orbitals was defined such that the trace of the occupation number matrices represents the $3d$ gross occupation. The exchange couplings in the $Pb_6Co_9(TeO_6)_5$ crystal were evaluated by performing the total energy calculations of various supercells with collinear spin configurations, which were then mapped onto a classical Heisenberg model to take into account the contribution of the exchange interactions from different neighbors.

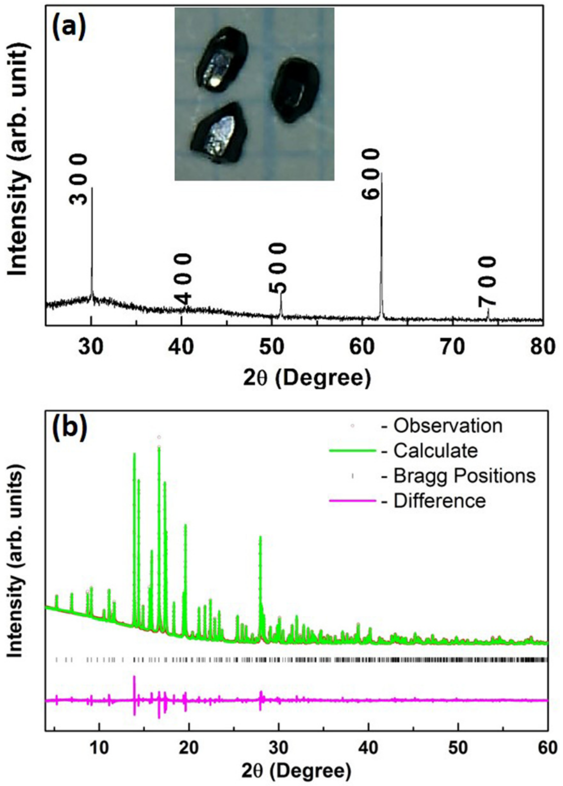

FIG. 2. (a) X-ray diffraction pattern of a $Pb_6Co_9(TeO_6)_5$ single crystal. The inset in (a) shows a cross-sectional image of the grown single crystals. (b) Rietveld refinement on XRD pattern of the powder form of the $Pb_6Co_9(TeO_6)_5$ crystal at room temperature.

IV. RESULTS AND DISCUSSION

A. Crystal structure

Figure 2(a) shows the XRD pattern of a single crystal in which a series of peaks can be indexed to the (h00) plane. The inset in Fig. 2(a) illustrates a typical cross-sectional optical microscopic image of the as-grown crystals. Figure 2(b) shows the XRD pattern of the ground single crystals of $Pb_6Co_9(TeO_6)_5$. Rietveld refinement of the XRD pattern is well fitted with a single phased hexagonal structure (space group $P6_322$). The refined lattice parameter values $a = b = 10.38808(4)$ Åand $c = 13.65051(5)$ Åare in good agreement with values in the literature [12]. The best fit was obtained with $\chi^2 \sim 4.77$ and $R_{wp} = 1.96\%$. The atomic positions obtained from Rietveld refinement are summarized in Table I. Additionally, the refined values of selected bond distances and angles are shown in the Supplemental Material (Tables S1 and S2) [20]. The obtained bond distances and bond angles are in good agreement with a previous report [12].

TABLE I. The atomic positions obtained from Rietveld refinement of the room-temperature XRD pattern of the powder form of $Pb_6Co_9(TeO_6)_5$ single crystals and the isotropic thermal parameters (B_{eq}).

Atom	Site	X	Y	Z	B_{eq}/A^2
Pb1	6g	0.2674(1)	0.2674(1)	0	1.04(1)
Pb2	6g	0.3866(1)	0	0	
Te1	4f	1/3	2/3	−0.0968(1)	0.003(14)
Te2	6h	0.1672(2)	0.3344(2)	1/4	
Co1	4f	1/3	2/3	0.1163(2)	0.04(2)
Co2	6h	0.1695(4)	0.3390(4)	−1/4	
Co3	2b	0	0	1/4	
Co4	6h	0.0112(3)	0.5056(3)	−1/4	
O1	12i	0.3357(10)	0.3231(12)	−0.1738(5)	0.16(6)
O2	12i	0.1696(14)	0.5011(12)	−0.1567(6)	
O3	12i	0.1661(13)	0.1775(12)	0.3233(4)	
O4	12i	0.3195(15)	0.4851(12)	0.3207(6)	
O5	12i	0.3490(7)	0.5255(7)	0.0017(13)	

B. X-ray photoelectron spectroscopy

The resultant XPS spectra for each element (Pb, Co, Te, and O) were deconvoluted and are shown in Fig. 3. The XPS spectrum of Te exhibits two distinct peaks, which are characteristics of the Te 3d electronic states [Fig. 3(a)] [21]. The peaks at binding energies of 576.8 and 587.3 eV correspond to the Te $3d_{5/2}$ and Te $3d_{3/2}$ states, respectively. The deconvoluted Te 3d spectrum suggests four peak components. The two strong peaks appearing at 576.9 and 587.4 eV confirm the presence of Te(VI) oxidation states, and relatively weak peaks at 574.9 and 585.8 eV confirm the existence of Te(II) oxidation states. The observed line shape and intensity contribution suggest that the Te(VI) oxidation state is more dominant in the sample than the Te(II) state. Similarly, the electronic structure of the Co element was probed by the XPS spectrum of the Co 2p level [Fig. 3(b)]. The peaks located at binding energies of 781.3 and 796.8 eV are characteristic of the $2P_{3/2}$ and $2P_{1/2}$ states, respectively, which are further deconvoluted into two spin-orbit doublets. The difference in binding energies between $2P_{3/2}$ and $2P_{1/2}$ states is found to be 15.5 eV. The deconvoluted $2P_{3/2}$ and $2P_{1/2}$ peaks demonstrate the presence of Co(II) and Co(III) ions which are consistent with literature reports for the Co(II) state at 780.8 eV and Co(III) state at 796.4 eV [22]. The peak area associated with the Co(II) ions shows a greater contribution than that of Co(III) ions. The two satellite peaks were observed at 786.6 and 802.3 eV adjacent to the respective two spin-orbit doublets. In general,

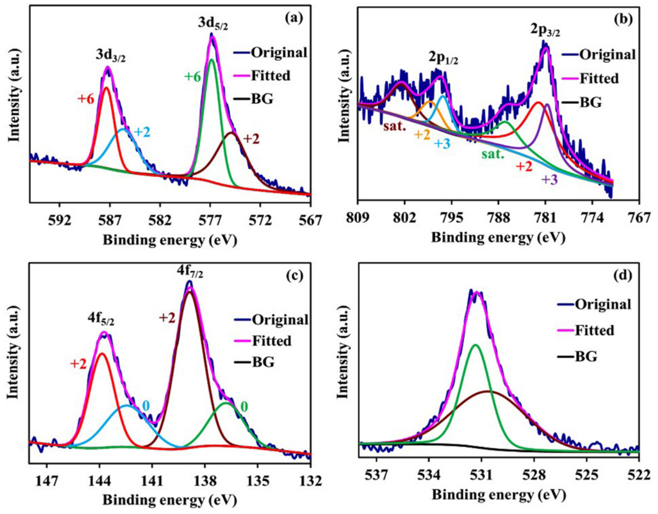

FIG. 3. XPS spectra of the $Pb_6Co_9(TeO_6)_5$ single crystal: (a) Te, (b) Co, (c) Pb, and (d) O elements.

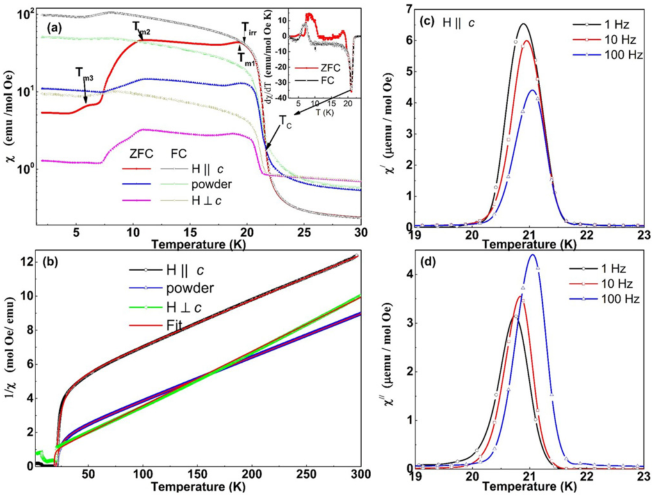

FIG. 4. (a) Magnetic susceptibility χ versus temperature data for a crystal of $Pb_6Co_9(TeO_6)_5$ in $H \parallel c$, $H \perp c$, and pulverized single-crystal samples measured at a magnetic field of 100 Oe. The inset in (a) shows an enlarged view of the first-order derivative of magnetic susceptibility data at low temperature. (b) Temperature dependence of inverse magnetic susceptibility. The red solid lines show the best fit by using a ferrimagnetic equation as described in the text for H at 100 Oe. (c) Real and (d) imaginary parts of the ac susceptibility as a function of temperature for different selected frequencies along $H \parallel c$ of a $Pb_6Co_9(TeO_6)_5$ single crystal in the absence of dc magnetic field.

these peaks will arise due to multielectronic excitations during the photoemission process [21]. The XPS spectrum of Pb [Fig. 3(c)] shows two strong peaks at the binding energy values of 138.9 and 143.6 eV, which correspond to the Pb $4f_{7/2}$ and Pb $4f_{5/2}$ states, respectively. These two Pb $4f$ peaks were deconvoluted with four components at 136.8, 138.9, 142.5, and 143.9 eV, respectively. The predominant peaks at 138.9 and 143.9 eV are attributed to the Pb(II) oxidation state, whereas the two peaks at 136.8 and 142.5 eV can be assigned to the zero-oxidation state of Pb [23]. The XPS spectrum of the O ions [Fig. 3(d)] exhibits a characteristic peak of the O 1s state that is fitted into two peaks with binding energy values at 530.4 and 531.2 eV, receptively. The peak (at 530.4 eV) with a broad contributed area is assigned to the metal-oxygen bonds in the crystal lattice, whereas the peak at 531.2 eV is ascribed to the adsorbed oxygen in the defect/vacancy sites of the lattice [21,22].

C. Magnetization and magnetic susceptibility

Figure 4(a) shows the temperature dependence of the magnetic susceptibility $\chi(T, H)$ (magnetization divided by applied magnetic field) measured at 100 Oe. The magnetization curves were measured in the temperature range of 2–400 K following zero-field-cooled (ZFC) and field-cooled (FC) modes by applying the magnetic field along the $H \parallel c$ and $H \perp c$ directions for the single crystal and average field for the powdered single crystal. However, $\chi(T, H)$ curves are shown in a limited temperature range, and the y axis is shown in log scale for clarity of the magnetic features at lower temperatures. The ZFC and FC curves bifurcated below the irreversibility temperature T_{irr}. The differences in the shapes of ZFC(T) and FC(T) magnetization curves at temperatures below T_{irr} are largely controlled by the freezing/pinning of magnetic domains. The magnetic curves show the anisotropic nature of the magnetic exchange interactions along the a-b plane and along the c axis, where magnetization is found to be higher for the $H \parallel c$ direction than the magnetization for the $H \perp c$ direction of the single crystal. The magnetization in the powder sample is found to be in between the values of the $H \parallel c$ and $H \perp c$ directions. In the case of the $H \parallel c$ measurement at 100 Oe, the ZFC curve at $T < T_{\text{irr}}$ indicated multiple anomalies, with a peak of magnetization at $T_{m1} \sim 19.3$ K and a subsequent increment of the magnetization indicated by a second peak at $T_{m2} \sim 11.1$ K. This is followed by a sharp decrease in the magnetization and a minor peak at $T_{m3} \sim 6.2$ K. On the other hand, the FC curve shows a monotonic increase below T_{irr} until the appearance of a peak at $T_m \sim 8$ K. The FC curve then sharply decreases and subsequently increases on further lowering of the temperatures below 5.5 K. The increase of the magnetization at lower temperatures can be associated with the spin reorientation effect in the crystal.

Similar features of the multiple magnetic anomalies in ZFC and FC curves were found for the measurements along the $H \perp c$ direction of the single crystal and powder sample, except the transition points are slightly different. The values of T_{irr}, T_{m1}, T_{m2}, T_{m3}, and T_m are found to be ~22, 18.8, 10.9, 5.95, and 8.6 K for the measurement along the $H \perp c$ direction and >50, 19.6, 11.2, 5.9, and 7.75 K for the measurement of the powder sample. The Curie temperature T_C of the samples was estimated by taking the first derivative of the ZFC and FC magnetization curves, and it is shown in the inset in Fig. 4(a) for the $H \parallel c$ measurement at 100 Oe. T_C is found at ~21.0 K (a sharp dip in the dM/dT vs T curves). It is found to be independent of the directions of applied magnetic field in the crystal and powder sample, irrespective of the ZFC and FC measurements. The magnetic behavior of the present compound below its T_C is not exactly identical to the features in the polycrystalline form of the $Pb_6Ni_9(TeO_6)_5$ and $Pb_6Co_9(TeO_6)_5$ compounds, which exhibited the signature of multiple magnetic transitions and weak FM spin order below its transition temperature at 25 K and AFM correlations with $\theta_{\text{CW}} \approx 35$ K at higher temperatures [10]. Recently, similar magnetic properties with multiple magnetic transitions were also observed below the ferrimagnetic (FIM) T_C of the honeycomb crystal-structured Ni_3TeO_6-type low-dimensional magnetic compound [24].

In order to determine the nature of the magnetic spin order around T_C, the inverse of dc (ZFC) magnetic susceptibility $\chi^{-1}(T)$ curves at an applied field of 100 Oe are plotted in Fig. 4(b). The curves for $T > T_C$ are best fit by the equation $\chi^{-1}(T) = (T - \theta_1)/C_{\text{eff}} - \xi/(T - \theta_2)$, which is applicable for the paramagnetic state of a ferrimagnetic material [25]. The fit parameters, as shown in Table II, confirm that the magnetic ground state of the honeycomb-structured compound $Pb_6Co_9(TeO_6)_5$ is a ferrimagnet at low applied fields and AFM exchange interactions (negative θ_1 with larger magnitude) among the spins dominate over the FM exchange interactions (positive θ_2 with smaller magnitude) at temperatures above T_C for $H \parallel c$ of the single crystal and also for the powdered sample [10]. The magnitude of θ_1 at an applied

TABLE II. Magnetic parameters obtained from fits by the ferrimagnetic equation for the $\chi^{-1}(T)$ data.

Direction	C_{eff} (emu/mol Oe)	μ_{eff} (units of μ_B)	θ_1 (K)	θ_2 (K)
$H = 100$ Oe				
$H \parallel c$	37.6	5.78	−176	17
$H \perp c$	31.39	5.28	−13	18
Powder sample	36.30	5.58	−68	15
$H = 10$ kOe				
$H \parallel c$	27.40	4.93	−78	19
$H \perp c$	34.6 (not a good fit)	5.55	−17	30
Powder sample	27.84	5.01	−27	15

magnetic field of 100 Oe is 10 times larger than that of θ_2 for $H \parallel c$, whereas the magnitude of θ_2 is found to be slightly larger than the magnitude of θ_1 for $H \perp c$. On the other hand, the magnitude of θ_1 is nearly 4.5 times θ_2 for powdered crystals, and it can be considered an average of the values for measurements along the $H \parallel c$ and $H \perp c$ directions. The fit parameters at an applied field of 10 kOe show that μ_{eff} values are slightly reduced in comparison to the values at $H = 100$ Oe and the AFM interactions seem to dominate over the FM interactions. Similar observations of the effect of the competition between the FM and AFM magnetic exchange interactions were reported for several compounds, including $Ba_3Cu_3In_4O_{12}$, [26] $Ba_3Cu_3Sc_4O_{12}$ [26], $Cu_3Y(SeO_3)_2O_2Cl$ [27], $CsCo_2Se_2$ [28], and $A_3T_2SbO_6$ (A = Li,Na; T = Co, Ni) [6,7].

The effect of spin frustration in the ground state is confirmed by the temperature dependence of the real $[\chi'(T)]$ and imaginary $[\chi''(T)]$ components of ac susceptibility. The measurement was performed at frequencies of 1, 10, and 100 Hz at a driving ac field amplitude of 1 Oe [Figs. 4(c) and 4(d)]. The peak around T_C in both the $\chi'(T)$ and $\chi''(T)$ curves shows a frequency shift and an estimated value of 0.081 K per decade of frequency change from the $\chi(T)$ curves, indicating a spin-glass-like feature [29]. Further, the magnitude of the $\chi''(T)$ curves is comparable to that of the $\chi'(T)$ curves. Such a feature is expected in a system of a FM/FIM ground state mixed with intrinsic spin frustration and disorder [30].

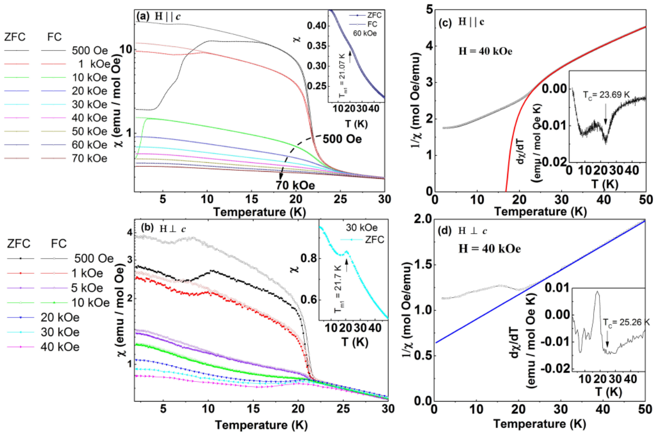

FIG. 5. Magnetic susceptibility versus temperature data for a crystal of $Pb_6Co_9(TeO_6)_5$ with various (a) $H \parallel c$ and (b) $H \perp c$. The artifact below T_C could be a small alignment problem in $H \perp c$. Inverse of the magnetic susceptibility as a function of temperature for (c) $H \parallel c$ and (d) $H \perp c$; the red and blue solid lines show the best fit using a ferrimagnetic equation and the Curie-Weiss law, respectively, for H at 40 kOe.

The effect of higher magnetic field on the spin order of the system is understood by measuring the ZFC and FC curves at magnetic fields up to 70 kOe in both the $H \parallel c$ and $H \perp c$ directions [Figs. 5(a) and 5(b), with the y axis in log scale]. It is observed that magnetic irreversibility between the FC and ZFC curves decreases and disappears for applied fields more than 10 kOe. The magnetic anomaly at T_{m1} slightly increases with magnetic field for both the $H \parallel c$ and $H \perp c$ directions. In contrast, the signature of the magnetic transitions at T_{m2} in the ZFC curves and at T_m in the FC curves shifts to lower temperature at higher magnetic fields. The minor peak at T_{m3} and other fluctuations observed in the low-field ZFC curves are absent at higher magnetic fields for measurement temperature down to 2 K. This can be attributed to the suppression of intrinsic spin disorder, including spin canting and spin pinning at the domain walls, at higher magnetic fields. The differences in the high-field ZFC and FC magnetization curves for the $H \parallel c$ and $H \perp c$ directions are clearly visible. In the case of $H \parallel c$, the increase in magnetization (with the reduction of irreversibility) extends down to low temperature with the increase of the magnetic field, which implies the saturation of the FM component at higher fields [10]. In the case of $H \perp c$, the features of the AFM spin order dominate in the ZFC/FC curves (without irreversibility, down to 2 K for $H \geqslant 10$ kOe) below T_{m1}, and a competition between the AFM and FM components at lower temperatures can be realized by noting the reappearance of increasing magnetization (the FM component). Interestingly, the $dMZFC/dT$ vs T curves at 40 kOe [insets in Figs. 5(c) and 5(d)] indicate the enhancement of T_C at higher applied fields. In order to clarify the magnetic field effect on the θ_1, θ_2, and μ_{eff} values, the $\chi^{-1}(T)$ curves at different fields were analyzed, and fitted curves for $H = 40$ kOe are shown in Figs. 5(c) and 5(d). The signature of the FIM feature remains at higher fields for $H \parallel c$, but it is transformed into a typical AFM feature at H above 10 kOe for the $H \perp c$ direction, and the $\chi^{-1}(T)$ curves for $T > T_C$ are perfectly fitted with the Curie-Weiss law $\chi^{-1}(T) = (T - \theta_{\text{CW}})/C_{\text{eff}}$. The calculated values of the magnetic parameters at higher fields are shown in Tables III and IV. In the case of the $H \parallel c$ direction, the AFM interactions (represented by θ_1) dominate over the FM interactions (represented by θ_2) in the balance of the exchange interactions above T_C, and the FM component gradually decreases at higher fields. This leads to a decrease in μ_{eff} at higher fields. The T_C value also shifts to higher values with magnetic fields. In the case of the $H \perp c$ direction, both μ_{eff} and the Curie temperature (which can also be defined as the Néel temperature T_N for the AFM case) are enhanced at higher fields.

The spin frustration parameter f of the system was estimated from the ratio of θ_1/T_C for $H \parallel c$ and θ_{CW}/T_C for the $H \perp c$ direction. It may be noted that θ_1 represents the relative strength of AFM interactions above T_C in the case of FIM spin order and θ_{CW} represents the strength of AFM

TABLE III. Magnetic parameters from the fit of the $\chi^{-1}(T)$ data using a ferrimagnetic equation for the magnetic field parallel to the c direction.

H (Oe)	θ_1 (K)	θ_2 (K)	C_{eff} (emu/mol Oe)	μ_{eff} (units of μ_B)	ζ (arbitrary units)	T_C (K)	$f = \lvert\theta_1/T_C\rvert$	T_{irr} (K)	T_{m1} (K)	T_{m2} (K)	T_{m3} (K)
100	−176.00	17.00	37.6	5.78	12.41	21.00	8.38	19.55	19.31	10.99	6.15
500	−79.00	19.00	28.0	4.99	6.02	21.10	3.74	18.00	13.20	10.40	6.00
1000	−77.90	19.19	27.4	4.93	5.99	21.10	3.69	10.00	9.50	6.70	
10 000	−82.48	16.90	26.5	4.85	9.52	21.88	3.77	5.30	3.40		
20 000	−74.67	15.20	26.0	4.81	9.46	22.48	3.32				
30 000	−62.22	15.10	23.7	4.59	7.31	23.02	2.70				
40 000	−55.63	12.00	22.4	4.47	5.82	23.17	2.40				
50 000	−59.79	10.96	23.0	4.52	8.63	24.10	2.48				
60 000	−114.80	−14.00	30.0	5.16	59.02	24.82	4.62				

interactions above T_C in the case of AFM spin order. Based on the fit parameters in Table II (using the ferrimagnetic equation), the value $f \approx 8.38$ for $H \parallel c$ at 100 Oe indicates strong frustration in the system, and the f value (using θ_1/T_C) at $H = 100$ Oe reduces to 0.62 and 3.23 for the $H \perp c$ in single crystal and powder sample, respectively. This indicates that spin frustration is large along the out-of-plane direction and the frustration parameter decreases at higher applied fields. In the case of the $H \perp c$ direction, the f value (using θ_{CW}/T_C) at $H = 100$ Oe is found to be 3.56, which is significantly reduced, and it stabilizes in the range of 1.06–1.21 at higher fields.

The high magnetic field induced effects are further understood from magnetic field dependent magnetization $M(H)$ measurements. The $M(H)$ curves of the samples at selected temperatures are shown in Figs. 6(a)–6(c). The isothermal $M(H)$ curves were measured in a field range of ±70 kOe and a temperature range of 2–25 K. The $M(H)$ curves at 2 K show the typical features of a ferrimagnet (a wide loop and lack of magnetic saturation at higher field, >2 T) for the $H \parallel c$ direction and the typical features of a canted AFM (a minor loop, as shown in the inset in Fig. 6(b), and a nonlinear nature along with a lack of magnetic saturation) for the $H \perp c$ direction of the single crystal. The $M(H)$ curve at 25 K [Fig. 6(a)] shows negligible nonlinearity without any loop for $H \parallel c$, and the same is also observed for the $H \perp c$ direction. This suggests a small effect of the short-range magnetic interactions for magnetic properties in the single crystal at temperatures above T_C. The features of the $M(H)$ curves for the powder sample (a reduced loop and lack of magnetic saturation at higher fields) are in between these two extreme cases of the field directions and are consistent with features observed in the $M(T)$ curves. At 2 K, the present material shows high coercivity ($H_C = 13$ kOe), and magnetic moment/Co ion reaches $\sim 5\mu_B$/f.u. at 70 kOe. The high coercivity in the single crystal is caused by magnetocrystalline anisotropy of the Co^{2+} ions. The experimental results confirmed the differences between the c axis anisotropy and the in-plane (a-b) anisotropy contribution, where the easy axis of the Co^{2+} ions can be considered along the c axis. The magnetic moment in our compound for $H \parallel c$ is close to the calculated magnetic moment of Co^{2+} in the high-spin state ($4.37\mu_B$, with a large orbital moment contribution of $1.71\mu_B$) in Sr_3CoIrO_6 [31], where the Co^{2+} moments are firmly aligned due to strong spin-orbit coupling (SOC) along the c axis (resembling Ising-like spin order). The temperature variation of the loop parameters (coercivity H_C and remanent magnetization M_R) in Fig. 6(d) shows that M_R

TABLE IV. Magnetic parameters from the fit of the Curie-Weiss law for the magnetic field perpendicular to the c direction.

H (Oe)	θ_{CW} (K)	C_{eff} (emu/mol Oe)	μ_{eff} (units of μ_B)	T_C or T_N (K)	$f = \lvert\theta_1/T_C\rvert$
100	−5.90	30.67	5.22	21.00	3.56
500	−17.90	35.70	5.63	20.74	1.16
1000	−18.00	33.30	5.44	20.82	1.16
10 000	−17.50	32.93	5.41	21.25	1.21
20 000	−19.52	35.18	5.59	23.67	1.21
30 000	−21.38	36.10	5.66	23.87	1.12
40 000	−23.40	37.03	5.74	24.82	1.06

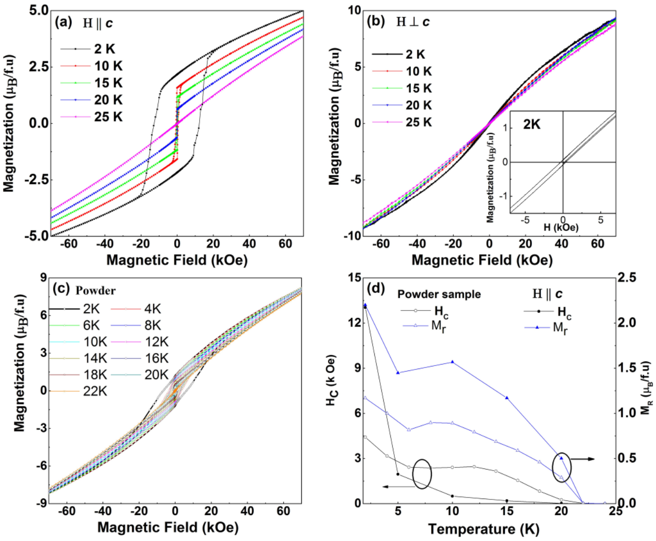

FIG. 6. Magnetization versus applied field at different selected temperatures for (a)$H \parallel c$ and (b) $H \perp c$ and (c) the crystal crushed powder sample. (d) Variation of the coercivity H_C (left axis) and the remanence magnetization M_r (right axis) with the measured temperature for $H \parallel c$ (solid symbols) and the powder sample (open symbols).

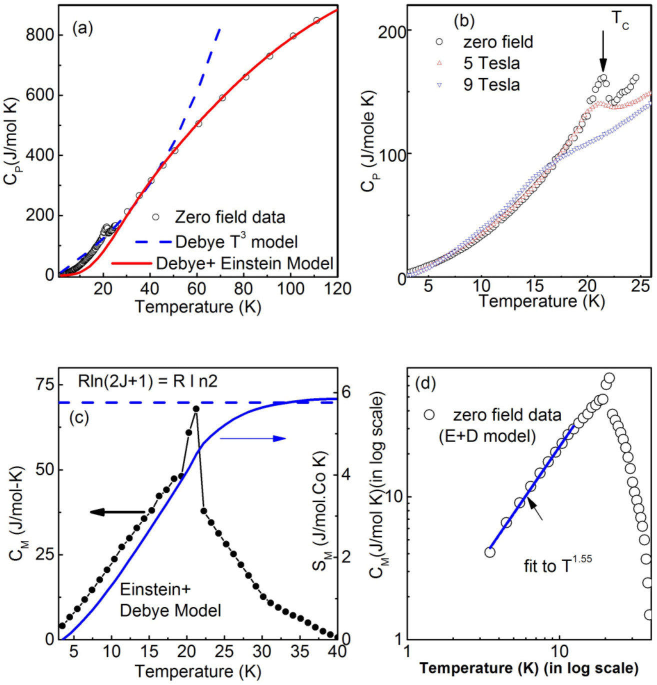

FIG. 7. (a) Temperature-dependent heat capacity C_P of $Pb_6Co_9(TeO_6)_5$ measured at zero magnetic field. (b) C_P data in the low-temperature regime for selected magnetic fields along the $H \parallel c$ direction. (c) Magnetic contribution C_M as a function of temperatures (on the left y axis) and the corresponding magnetic entropy S_M (on the right y axis). (d) Fit of the power law in the low-temperature regime of the C_M vs T curve in log-log scale.

in the single crystal for $H \parallel c$ is higher than the values in the powder sample. On the other hand, the H_C values in the single crystal are drastically reduced for temperatures above 2 K and become lower than the values in the powder sample for temperatures > 5 K. The temperature variation of both H_C and M_R is nonmonotonic, with a signature of the local minimum at about 5 K and a broad hump in the temperature range of 10–15 K. The features are similar to the low-field ZFC $M(T)$ curves, and they can be correlated to a spin reorientation effect for some of the Co^{2+} ions in the magnetic ground state of the crystal at low temperatures.

D. Heat capacity

The heat capacity C_p was measured for a $Pb_6Co_9(TeO_6)_5$ single crystal at zero magnetic field [Fig. 7(a)] and in the presence of applied magnetic fields [Fig. 7(b)] for the $H \parallel c$ direction. As shown in Fig. 7(b), the $C_p(T)$ curve in zero applied magnetic field exhibits a sharp peak at ∼21 K, which is a signature of a true second-order-type magnetic phase transition and agrees with the ferrimagnetic transition observed in low-field dc magnetization curves. The sharp peak of the $C_p(T)$ curve at zero field is gradually suppressed and broadened and shifted to lower temperatures on increasing the field value from 50 to 90 kOe. In a true long-range-ordered ferro- or ferrimagnet, a second-order phase transition occurs only at zero field as the order parameter, i.e., spontaneous magnetization develops above T_C in magnetic fields, and the transition switches into a crossover magnetic phase in the presence of finite field. This results in a broadening or smearing out of the $C_p(T)$ peak at T_C at higher magnetic fields. Such a magnetic field induced phenomenon can be expected due to Zeeman splitting of the $J = \frac{1}{2}$ energy levels at low temperatures [32]. The absence of any additional peak in the $C_p(T)$ curve, except for a strong peak close to T_C, suggests that the anomalies observed in the low-field ZFC magnetization curves at temperatures below T_C are not associated with any long-range magnetic phase transition.

The measured $C_P(T)$ curve of a magnetic material can be expressed as the sum of the electronic contribution ($C_{\mathrm{el}} = \gamma$ T), the phonon/lattice contribution ($C_{\mathrm{ph}} = \beta T^3$), and the magnetic contribution C_M. In the absence of nonmagnetic materials isostructural to the present compound, the nonmagnetic (electronic and phonon) contributions are estimated by using the Debye model [$C_P(T) = \gamma T + \beta T^3$]. In the first step, the values of γ and β are estimated by a linear fitting of the C_p/T vs T^2 curve in the temperature range between 23 and 45 K [shown in Fig. 7(a)]. The best fit yields $\beta = 0.00125$ J/mol K^4. However, the value $\gamma \approx 5.684$ J/mol K^2 (the intercept is on the C_P/T axis and $T^2 = 0$) is physically not acceptable because the electronic contribution γ is expected to be negligible for insulating materials, which is the case for the present material. The extrapolation of the high-temperature fit data is seen to be higher than the experimental data at lower temperatures, which is not feasible. Hence, it is realized that application of a simple Debye model is insufficient to accurately determine nonmagnetic (electronic and phonon) contributions to the heat capacity of the material. In such a case, a combination of the Debye ($C_{\mathrm{V\,Debye}}$) model and Einstein ($C_{\mathrm{V\,Einstein}}$) model [33] was found to be a better description ($\gamma = 0$) for the $C_P(T)$ curve. The Debye model and Einstein model correspond to acoustic and optic modes of the lattice vibration, respectively, are and connected by the following expressions:

$$C_{\mathrm{ph}} = k\,C_{\mathrm{V\,Debye}} + (1-k)\,C_{\mathrm{V\,Einstein}},$$

$$C_{\mathrm{V\,Debye}} = 9nR\left(\frac{T}{\Theta_{\mathrm{D}}}\right)^3 \int_0^{\Theta_{\mathrm{D}}/T} \frac{x^4 e^x}{(e^x-1)^2}\,dx,$$

$$C_{\mathrm{V\,Einstein}} = 3nR\left(\frac{\Theta_{\mathrm{E}}}{T}\right)^2 \frac{e^{\frac{\Theta_{\mathrm{E}}}{T}}}{\left(e^{\frac{\Theta_{\mathrm{E}}}{T}}-1\right)^2}.$$

Here, Θ_{D} is the Debye temperature, Θ_{E} is the Einstein temperature, R is the molar gas constant, and k represents the weight percentage of the lattice contributions to the $C_P(T)$ data given by the Debye and Einstein terms. The fit of the C_p(T) data is excellent when the above expression is applied between 30 and 120 K and further extrapolated down to 2 K. The best fit [shown in Fig. 7(a)] reveals $\Theta_{\mathrm{D}} = 167(6)$ K and $\Theta_{\mathrm{E}} = 359(4)$ K, with $k = 0.51$, and 51% of the total heat capacity corresponds to the Debye (D) term, and 49% corresponds to the Einstein (E) term. Ali *et al.* [33] obtained contributions to the total heat capacity of 41% from the Debye term and 59% from the Einstein term by applying the same model, although on a different kind of layered material which is a noncentrosymmetric superconductor with large SOC. The magnetic contribution C_M to the heat capacity in our sample was obtained by subtracting the phonon contribution C_{ph} from the measured $C_p(T)$ data. The obtained C_M vs T curve is shown in Fig. 7(c) (left y axis). The numerical integration of the C_M/T vs T curve (not shown) was used to calculate the magnetic entropy $S_M(T)$ curve, which is also shown in Fig. 7(c) (right y axis). The maximum magnetic entropy is attained at 35 K and has a value of 5.84 J/mol Co K; it is in good agreement with the theoretical maximum value of 5.76 J/mol Co K according to $R\ln(2J+1) = R\ln 2$, where the magnetic moment per Co^{2+} ion can be defined by $J = \frac{1}{2}$ instead of $S = \frac{3}{2}$ and the magnetic order of the Co^{2+} ions is affected by strong spin-orbit coupling. From magnetic and heat capacity measurements of the $Ba_3CoTa_2O_9$ compound, Ranjith *et al.* [32] suggested that Co^{2+} ions can adopt the $J = \frac{1}{2}$ state at low temperatures and the $S = \frac{3}{2}$ state at higher temperatures. The entropy at T_C ($\sim$21 K) is 4.37 J/mol K, which is found to be 75% of the total entropy; the remaining 25% of the entropy is released above T_C. This is due to short-range magnetic correlation at temperatures above T_C, and it is seen as a common feature for the existence of spin frustration in magnetic materials [34,35]. On the other hand, the C_M(T) data under zero magnetic field at low temperature followed a power law: $C_M(T) \approx AT^n$, where A is constant and n is the exponent. The fit of the C_M(T) data [Fig. 7(d), in log-log scale] provides $n \approx 1.55$, and it closely obeys the $T^{3/2}$ law, which is a characteristic feature of the spin wave contribution in a long-range ferro- or ferrimagnetic compound [36,37].

V. DENSITY FUNCTIONAL THEORY

Because of the lack of any prior electronic structure calculations for $Pb_6Co_9(TeO_6)_5$, we begin by analyzing the results from a nonmagentic LDA calculation. In a simplified model, each Co^{2+} ion is surrounded by a slightly distorted octahedron of O^{2-} ions, such that the spin-up channels of both the t_{2g} and e_g orbitals are fully filled with five electrons and the remaining two electrons occupy the spin-down channel of the t_{2g} state. The nonmagnetic total and orbital resolved densities of states (DOSs) of $Pb_6Co_9(TeO_6)_5$ are depicted in Fig. 8. The presented part of the valence band close to the Fermi level is predominantly composed of Co 3d and O 2p states belonging to CoO_6 octahedra. The states belonging to Pb and Te lie below -7.5 eV and therefore are well separated from the CoO_6 states. We note that the LDA analysis, due to the well-known inadequate treatment of the strong Coulomb correlation of the 3d orbitals, results in a metallic DOS, in contrast to the experimentally insulating ground state. Therefore, the orbital dependence of the Coulomb and exchange interactions is taken into account in a mean-field-like approximation using the LSDA+U approach, which opens an insulating gap, with $U = 5$ eV. To evaluate the exchange couplings, we performed LSDA+U total energy calculations for various collinear spin configurations and mapped the energy differences onto a classical Heisenberg model to obtain the total exchanges J_i. The obtained results are tabulated in Table V, and a cartoon depicting the considered exchange pathways is presented in Fig. 9.

In the calculation, we start with the nearest-neighbor (NN) distance and bond angles of Co ions using the values from Rietveld refinement (shown in Tables S1 and S2 in the Supplemental Material [20]). The first exchange J_1 is calculated in $Pb_6Co_9(TeO_6)_5$, wherein the neighboring Co atoms are separated by 2.9358 Å. The NN Co (Co2, Co4) ions form a regular honeycomb-type lattice (see Fig. 9), with the superexchange pathway Co-O-Co of the angle very close to 90°. According to the Goodenough-Kanamori rules [38,39], the bond angles of Co-O-Co around 90° favor FM coupling, and the bond angle of Co-O-Co around 120°–122° favors AFM coupling. The nature of exchange interactions in our LDA+U calculations is shown in Table V. We obtained strong FM coupling for the NN superexchange pathway (Co-O-Co) of Co (Co2, Co4) ions, giving rise to J_1. There is a second, albeit heavily distorted, honeycomb-type lattice in the $Pb_6Co_9(TeO_6)_5$ crystal whose edges are built up from two first-NN J_1 and two second-NN J_2 exchanges, both on the *ab* plane, and two third-NN J_3 exchanges that distort the lattice along the c axis. We also obtain FM exchange coupling for J_2 and AFM exchange coupling strength for J_3. Here, the superexchange pathway Co-O-Co of Co (Co2, Co3) ions is

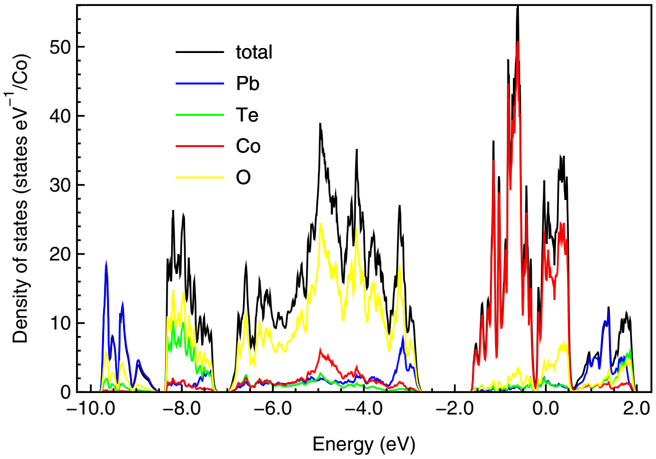

FIG. 8. Total and orbital projected densities of states of $Pb_6Co_9(TeO_6)_5$ calculated using DFT, employing the LDA exchange-correlation functional. The valence band close to the Fermi level (-1.6 to 0.5 eV) consists predominantly of cobalt 3d states, with a small admixture of oxygen 2p states. Between -2.7 and-7 eV, the weights are reversed, with predominantly oxygen 2p admixed with small amounts of cobalt 3d. The primary weights of the remaining Te and Pb atoms are found below -7 eV and above 0.5 eV.

TABLE V. Calculated exchange couplings using the full-potential local orbital code and the LDA+U method with $U = 5$ eV.

J	Co ions	Co-Co distance (Å)	$J_{\mathrm{LDA+U}}$ (K)
J_1	Co2-Co4	2.9358	203 (FM)
J_2	Co2-Co3	3.0391	217 (FM)
J_3	Co1-Co4	3.5724	−52 (AFM)
J_4	Co1-Co1	3.5889	225 (FM)
J_5	Co4-Co4	5.0411	25 (FM)
J_6	Co2-Co2	5.1277	−208 (AFM)
J_7	Co3-Co4	5.1965	31 (FM)

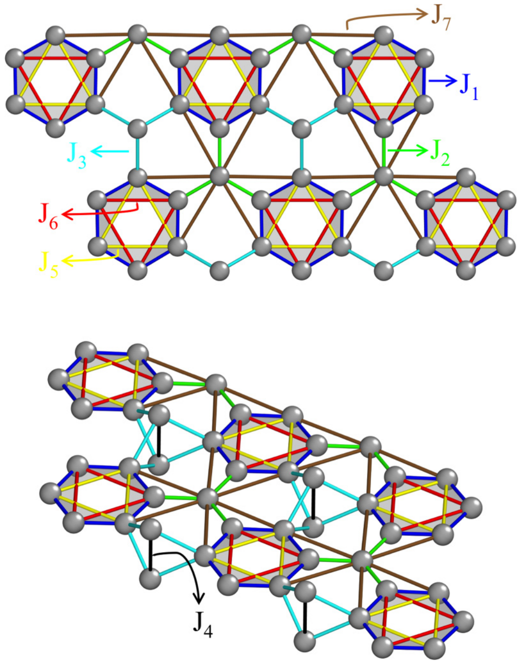

FIG. 9. Top view of the *ab* plane (top panel) and side view (bottom panel) of the various exchange couplings (J_1 to J_7) in $Pb_6Co_9(TeO_6)_5$ calculated using band structure calculations. Except for the Co atoms forming the J_4 exchange, all other Co atoms (solid spheres) lie in the *ab* plane.

close to 90°, giving rise to J_2, but the superexchange pathway Co-O-Co of Co (Co1, Co4) ions close to 120° gives rise to J_3. Next, couplings J_3 and J_4 together form two edge-sharing nearly equilateral triangles. The difference in the bond lengths is only 0.01 Å. This structural feature invokes a geometrical frustration, resulting in a FM J_4. The exchange couplings J_5 and J_6 are also in plane and fall inside the regular honeycomb-type lattice, forming second-neighbor interactions within the regular honeycomb lattice. Curiously, J_5 turned out to be FM and small, while J_6 turned out to be AFM and large in our calculations. While all other couplings are robust upon the change in U, it must be noted that J_5 and J_6 are somewhat sensitive, with both couplings sometimes becoming AFM for certain U values. This aspect could be related to the negative Curie-Weiss constant, along with the FM behavior, seen in the experiments. Basically, a large negative theta implies dominant AFM coupling in the system.

The exhibition of ferrimagnetic features, i.e., FM behavior (ZFC/FC hysteresis) and negative θ_1 or θ_{CW}, in a system does not always require two different types of magnetic ions. The same magnetic ions, e.g., Co^{2+} in the present system, with different orientations from different lattice sites may be sufficient for the origin of ferrimagnetism. Although we do not observe a typical metamagnetic transition, i.e., a distinct step jump in the $M(H)$ curve for H up to 7 T, a spin-flop transition was noted in the polycrystalline form of similar materials at relatively higher magnetic field ($\geqslant$15 T) [10]. The ferrimagnetic ground state in our single-crystalline sample can be realized by noting the uncompensated magnetic moments between the different magnetic sublattices at nearly zero magnetic field. Our estimation from the extrapolation of low-field magnetization data at 2 K gives a value of the order of $0.08\mu_B$/f.u. for the $H \parallel c$ direction and nearly $0.0\mu_B$/f.u. for the $H \perp c$ direction of the single crystal and nearly $0.05\mu_B$/f.u. for the powdered sample. In our opinion, there are two major sources of the uncompensated magnetic moments in the system. The first possibility is a zigzag-type spin order due to buckling of A- and B-type layers in the hexagonal structure with different orientations of the Co^{2+} moments [6]. Additionally, Co^{2+} moments in the *a*-*b* plane can form a canted spin structure due to the presence of Dzyaloshinskii-Moriya (DM) anisotropic interactions, and DM interactions are favorable due to strong spin-orbit coupling in the system [10]. The dominating ferrimagnetic state in the low-field regime also suggests that the spin orientation of the Co^{2+} ions from different (neighboring) lattice sites about the c axis is not collinear. The noncollinearity or spin canting among the Co^{2+} ions from different (neighbor) lattice sites gives rise to unequal magnetic contributions and ferrimagnetism. Our theoretical calculations provided a combination of positive and negative exchange interactions with different strengths from different neighbors of Co^{2+} ions. Considering experimental results from dc magnetization measurements (dominating ferro-/ferrimagnetic state at lower fields and dominating AFM state at higher fields), it can be suggested that the in-plane and out-of-plane spin order of the Co^{2+} ions is affected by the magnitude of the applied magnetic field. The in-plane magnetic disorder is reduced, and Co^{2+} moments are oriented at higher fields to stabilize the AFM spin order.

One more important fact (see Tables II–IV) is that $\mu_{\rm eff}$ (the effective paramagnetic moment) of the Co ion was found to be higher than the spin-only value of the Co^{2+} ion in the high-spin state ($S = \frac{3}{2}$, $g_S = 2$, $\mu_{\rm eff} = 3.83\mu_B$). Although the XPS spectra indicated non-negligible signals from Co^{3+} ions in addition to Co^{2+} ions and the four Co crystallographic sites might have a contribution from Co^{3+} states, the high value of the magnetic moment from experiments suggests that Co ions can be assumed to be purely in the 2+ valence state and the magnetic contribution of the Co^{3+} ions (low-spin state with zero moment) is zero. The $\mu_{\rm eff}$ of the Co^{2+} ion in the present system was found to be $5.78\mu_B$ and $5.28\mu_B$ from the fit of the ferrimagnetic equation for $H = 100$ Oe along the $\parallel c$ and $\perp c$ directions, respectively. Here, $\mu_{\rm eff}$ has been reduced to $4.78\mu_B$ (from the fit using the ferrimagnetic equation) and increased to $5.74\mu_B$ (from the fit using the Curie-Weiss law) for $H = 40$ kOe along the $\parallel c$ and $\perp c$ directions, respectively. This indicates the existence of strong SOC for Co^{2+} ions in the octahedrally coordinated environment of a honeycomblike structure [6,10,31,32,34]. In the presence of strong SOC, the g factor differs from the free-electron spin value of 2 because of mixing of different J states, and it is temperature dependent. According to earlier reports [6,32], the g factor can be expected in the ranges of ≈3–3.87 and 3.84–4.6 for the $H \parallel c$ and $\perp c$ directions, respectively. $\mu_{\rm eff}$ can be found in the range of $2.68\mu_B$–$6\mu_B$ by using an average $g = 3.1$ [32], and it is within the range of our experimental values. The variation of $\mu_{\rm eff}$ with magnetic fields can be correlated to the strength of *LS* coupling in showing the Zeeman splitting of J states.

As described earlier, Co1 ions can be connected to Co2, Co3, and Co4 ions through nonmagnetic Te^{6+} ($4d^{10}$) ions by weak interlayer (Co-O-Te-O-Co) superexchange couplings. There is a possibility that the differences in magnetic moment and spin order of the Co^{2+} ions for H along the$\parallel c$ and $\perp c$ directions can be affected by such weak interlayer superexchange couplings via Te^{6+} ions. Te^{6+} in the ionic group of the TeO_6 octahedron pulls ($4s$) electrons from oxygen more than the edge-sharing neighboring CoO_6 octahedron. This leaves the $3d$-$4s$ gap of the CoO_6 octahedra negligibly small. This gives rise to strong SOC in the electron density distribution of CoO_6 octahedra. Similar to the present compound, many compounds, e.g., Sr_3NiIrO_6 and Sr_3CoIrO_6, display an in-plane hexagonal spin structure and out-of-plane (quasi-one-dimensional) spin chains [31]. The main feature of such systems is the exhibition of complex temperature-dependent magnetic transitions and the nonuniqueness of the intrachain magnetic exchange interactions of either the FM or AFM type. The DFT calculations, including SOC and electron correlation, accounted for the higher stability of the AFM ground state over the FM state in Sr_3CoIrO_6 compared with Sr_3NiIrO_6 due to the fact that the Co^{2+} ion carries huge orbital moment compared with that in Ni^{2+} ion. In such systems, an intrinsic spin frustration due to the competition between FM and AFM exchange always exists. This is supported theoretically by the DFT calculations and experimentally by the observation of a spin-glass-like feature in the ac susceptibility measurements.

VI. CONCLUSION

We have studied the structural, magnetic, and thermodynamics properties of a single crystal and powdered crystals of the $Pb_6Co_9(TeO_6)_5$ compound. The system showed irreversibility between ZFC and FC curves below the paramagnetic to ferrimagnetic transition temperature ($T_C \approx 21$ K) due to anisotropy effects. The uncompensated magnetic moment in the ferrimagnetic ground state is assumed to be contributed largely by a zigzag-type spin order due to buckling of A- and B-type layers in the hexagonal structure with different orientations of the Co^{2+} moments and a complex spiral (canted) spin structure of the Co^{2+} moments. The heat capacity measurement at zero field confirmed a second-order-type ferrimagnetic transition at 21 K, and the observed anomalies in the low-field dc magnetization (ZFC) curves below T_C are not associated with any true long-range magnetic phase transition. The $C_P(T)$ curve at zero magnetic field is fitted by a combined model of the Debye term (51%) and the Einstein term (49%). The analysis of the magnetic contribution to the heat capacity suggested that the magnetic moment per Co^{2+} ion adopts $J = \frac{1}{2}$, instead of $S = \frac{3}{2}$, and the system has strong SOC. Magnetization studies revealed a highly anisotropic nature of the in-plane (a-b) and out-of-plane ($\parallel c$) exchange interactions. The magnetic properties depend on the directions of the applied field in the single crystal and also on the nature of the sample, either a single crystal or powdered crystals. The compound seems to be stabilized in the AFM state at higher applied fields. T_C at 21 K from the low-field magnetization curve showed an enhancement up to 24.82 K by increasing the applied magnetic field to 6 T. These features confirm the presence of spin frustration in the long-range magnetic ground state of the system. The spin frustration in the magnetic ground state is possible due to the competition between the FM and AFM superexchange interactions (Co-O-Co), originating from different nearest neighbors of Co^{2+} ions and the geometric distortion in both the a-b planes and c direction of the regular honeycomb-type lattice structure of the $Pb_6Co_9(TeO_6)_5$ compound. The spin frustration order parameter f was found to be very high (8.38) for $H \parallel c$ at 100 Oe, and the value decreased to the range of 2.48–3.74 in the high-field regime. On the other hand, the spin frustration parameter was about 3.56 at 100 Oe for the $H \perp c$ direction, and the value stabilized in the range of 1.06–1.16 in the high-field regime. The competition between FM and AFM exchange interactions and the existence of spin frustration in the magnetic ground state illustrated a spin-glass-like feature for the $H \parallel c$ direction.

ACKNOWLEDGMENTS

I.P.M thanks the Department of Science and Technology (IN) in India for the support from INSPIRE faculty Award No. DST/INSPIRE/04/2016/002275 (IFA16-PH171). K.S. acknowledges the financial assistance from University Grants Commission, India, for D. S. Kothari Postdoctoral Fellowship (DSKPDF) Award No. F.4-2/2006 (BSR)/PH/18-19/0099. R.N.B. acknowledges a research grant from Department of Science and Technology-SERB (IN) (Grant No. CRG/2019/000505) to participate in this research work. R.S. acknowledges financial support provided by the Ministry of Science and Technology in Taiwan under Project No. MOST-108-2112-M-001-049-MY2 and Sinica funded i-MATE financial Support AS-iMATE-109-13.

---

[1] A. Banerjee, C. A. Bridges, J.-Q. Yan, A. A. Aczel, L. Li, M. B. Stone, G. E. Granroth, M. D. Lumsden, Y. Yiu, J. Knolle, S. Bhattacharjee, D. L. Kovrizhin, R. Moessner, D. A. Tennant, D. G. Mandrus, and S. E. Nagler, Nat. Mater. **15**, 733 (2016).

[2] S. Derakhshan, H. L. Cuthbert, J. E. Greedan, B. Rahaman, and T. Saha-Dasgupta, Phys. Rev. B **76**, 104403 (2007).

[3] M. A. Evstigneeva, V. B. Nalbandyan, A. A. Petrenko, B. S. Medvedev, and A. A. Kataev, Chem. Mater. **23**, 1174 (2011).

[4] J. Chaloupka, G. Jackeli, and G. Khaliullin, Phys. Rev. Lett. **105**, 027204 (2010).

[5] Y. Singh and P. Gegenwart, Phys. Rev. B **82**, 064412 (2010).

[6] H. Liu, J. Chaloupka, and G. Khaliullin, Phys. Rev. Lett. **125**, 047201 (2020).

[7] E. A. Zvereva, M. I. Stratan, Y. A. Ovchenkov, V. B. Nalbandyan, J.-Y. Lin, E. L. Vavilova, M. F. Iakovleva, M. Abdel-Hafiez, A. V. Silhanek, X.-J. Chen, A. Stroppa, S. Picozzi, H. O. Jeschke, R. Valenti, and A. N. Vasiliev, Phys. Rev. B **92**, 144401 (2015).

[8] W. Schmidt, R. Berthelot, L. Etienne, A. Wattiaux, and M. A. Subramanian, Mater. Res. Bull. **50**, 292 (2014).

[9] N. Bhardwaj, A. Gupta, and S. Uma, Dalton Trans. **43**, 12050 (2014).

[10] B. Koteswararao, T. Chakrabarty, T. Basu, B. K. Hazra, P. V. Srinivasarao, P. L. Paulose, and S. Srinath, Sci. Rep. **7**, 8300 (2017).

[11] P. R. Baral, N. Ahmed, J. Kumar, S. Nair, and R. Nath, J. Alloys Compd. **711**, 568 (2017).

[12] C. Artner and M. Weil, Acta Cryst. E **68**, i71 (2012).

[13] F. Zschocke and M. Vojta, Phys. Rev. B **92**, 014403 (2015).

[14] Y. Kubota, H. Tanaka, T. Ono, Y. Narumi, and K. Kindo, Phys. Rev. B **91**, 094422 (2015).

[15] P. A. Lee, Science **321**, 1306 (2008).

[16] G. Baskaran, S. Mandal, and R. Shankar, Phys. Rev. Lett. **98**, 247201 (2007).

[17] K. Koepernik and H. Eschrig, Phys. Rev. B **59**, 1743 (1999).

[18] I. Opahle, K. Koepernik, and H. Eschrig, Phys. Rev. B **60**, 14035 (1999).

[19] J. P. Perdew and Y. Wang, Phys. Rev. B **45**, 13244 (1992).

[20] See Supplemental Material at http://link.aps.org/supplemental/10.1103/PhysRevB.104.174442 for details of the refined values of selected bond distances and angles in Tables S1 and S2.

[21] R. J. Kriek, M. Z. Iqbal, B. P. Doyle, and E. Carleschi, ACS Appl. Energy Mater. **2**, 4205 (2019).

[22] M. Smyrnioti and T. Ioannides, in *Cobalt*, edited by K. Maaz (IntechOpen, 2017), Chap. 3, pp. 49–69.

[23] J. Luo, M. Sun, C. L. Ritt, X. Liu, Y. Pei, J. C. Crittenden, and M. Elimelech, Environ. Sci. Technol. **53**2075 (2019).

[24] I. P. Muthuselvam, K. Saranya, R. Sankar, R. N. Bhowmik, and L. Kavitha, J. Appl. Phys. **128**, 123902 (2020)

[25] R. N. Bhowmik, J. Magn. Magn. Mater. **323**, 311 (2011).

[26] M. Kumar, S. E. Dutton, R. J. Cava, and Z. G. Soos, J. Phys.: Condens. Matter **25**, 136004 (2013).

[27] K. V. Zakharov, E. A. Zvereva, P. S. Berdonosov, E. S. Kuznetsova, V. A. Dolgikh, L. Clark, C. Black, P. Lightfoot, W. Kockelmann, Z. V. Pchelkina, S. V. Streltsov, O. S. Volkova, and A. N. Vasiliev, Phys. Rev. B **90**, 214417 (2014).

[28] F. von Rohr, A. Krzton-Maziopa, V. Pomjakushin, H. Grundmann, Z. Guguchia, W. Schnick, and A. Schilling, J. Phys.: Condens. Matter **28**, 276001 (2016).

[29] S. Pakhira, C. Mazumdar, A. Basu, R. Ranganathan, R. N. Bhowmik, and B. Satpati, Sci. Rep. **8**, 14870 (2018).

[30] E. Christou, B. Uchoa, and F. Krüger, Phys. Rev. B **98**, 161120(R) (2018).

[31] X. Ou and H. Wu, Sci. Rep. **4**, 4609 (2014).

[32] K. M. Ranjith, K. Brinda, U. Arjun, N. G. Hegde, and R. Nath, J. Phys.: Condens. Matter **29**, 115804 (2017).

[33] M. N. Ali, Q. D. Gibson, T. Klimczuk, and R. J. Cava, Phys. Rev. B **89**, 020505(R) (2014).

[34] I. P. Muthuselvam, R. Sankar, A. V. Ushakov, G. N. Rao, S. V. Streltsov, and F. C. Chou, Phys. Rev. B **90**, 174430 (2014).

[35] S. Sahling, J. E. Lorenzo, G. Remenyi, C. Marin, V. L. Katkov, and V. A. Osipov, Sci. Rep. **10**, 10909 (2020).

[36] W. N. Lawless, Phys. Rev. Lett. **36**, 478 (1976).

[37] I. P. Muthuselvam, R. Sankar, A. V. Ushakov, W. T. Chen, G. Narsinga Rao, S. V. Streltsov, S. K. Karna, L. Zhao, M.-K. Wu, and F. C. Chou, J. Phys.: Condens. Matter **27**, 456001 (2015).

[38] J. B. Goodenough, Phys. Rev. **100**, 564 (1955).

[39] J. Kanamori, J. Phys. Chem. Solids **10**, 87 (1959).